Chemical Science Page 2 of 48

# Real-Time Capture of Nuclear Motions Influencing Photoinduced Electron Transfer

Pyosang Kim,\*,1,2 Subhangi Roy,3 Andrew J. S. Valentine,4 Xiaolin Liu,4 Sarah Kromer,3 Tae Wu Kim,1 Xiaosong Li, \*,4 Felix N. Castellano\*,3 and Lin X. Chen\*,1,2

<sup>1</sup>Chemical Sciences and Engineering Division, Argonne National Laboratory, Lemont, IL 60439

<sup>2</sup>Chemistry Department, Northwestern University, Evanston, IL 60208

<sup>3</sup>Chemistry Department, North Carolina State University, Raleigh, NC 27695-8204

<sup>4</sup>Chemistry Department, University of Washington, Seattle, WA 98195

### Abstract

Although vibronic coupling phenomena have been recognized in the excite state dynamics of transition metal complexes, its impact on photoinduced electron transfer (PET) remains largely unexplored. This study investigates coherent vibrational wavepacket (CVWP) dynamics during PET processes in a covalently linked electron donor-acceptor complex featuring a cyclometalated Pt(II) dimer as the donor and naphthalene diimide (NDI) as the acceptors. Upon photoexciting the Pt(II) dimer electron donor, ultrafast broadband transient absorption spectroscopy revealed direct modulation of NDI radical anion formation through certain CVWP motions and correlated temporal evolutions of the amplitudes for these CVWPs with the NDI radical anion formation. These results provide clear evidence that the CVWP motions are the vibronic coherences coupled to the PET reaction coordinates. Normal mode analysis identified that the CVWP motions originate from vibrational modes associated with the dihedral angles and bond lengths between the planes of the cyclometalating ligand and the NDI, the key modes altering their  $\pi$ -interaction, consequently influencing PET dynamics. The findings highlight the pivotal role of vibrations in shaping the favorable trajectories for the efficient PET processes.

Chemical Science Page 4 of 48

## Introduction

Natural photosynthetic reaction centers set examples for nearly 100% quantum efficiency in photoinduced charge separation, driving biochemical reactions responsible for storing the energy necessary to sustain life on Earth.1 The detection of coherent vibrational wavepacket (CVWP) motions within the reaction centers stimulated investigations on the role of nuclear motions in achieving highly efficient charge separation.<sup>2-4</sup> Subsequent studies have identified the CVWP motion as an electronic-vibrational (vibronic) coherence that persists over the timescale of the photoinduced charge separation.<sup>5-7</sup> It was suggested that the vibronic coherences arise from the resonance between electronic and vibrational energies, facilitating vibronic wavefunction delocalization across the exciton and charge transfer (CT) state and thus boosting the efficiency of charge separation.<sup>8, 9</sup> Vibronic coherence has also garnered significant attention for its potential role in photoinduced electron transfer (PET), a fundamental process in artificial solar energy conversion systems. 10-12 For instance, a 100 fs PET process in a blend of poly(3-hexylthiophene) (P3HT) and fullerene coincided with the emergence of CVWP motions attributed to the vibrations of fullerene, highlighting the interplay of electron and vibrational motions during the primary charge separation.<sup>13</sup> Furthermore, it was experimentally demonstrated that the vibronic coherence directly influences the photocurrent generation in other organic heterojunctions solar cells.<sup>14</sup> These observations suggest that the vibronic coherence between the electron donor and acceptor could play a pivot role in facilitating efficient PET dynamics in artificial systems.

The aforementioned studies demonstrating the role of vibronic coherence in PET processes has inspired the present study on an electron donor-acceptor system featuring a transition metal complex (TMC) as the donor. The light absorption process directly gives rise to a CT state in the TMCs, either from metals to ligands or vice versa. The CT transition generates a redox potential in the excited state, which makes the TMCs promising to drive the primary ET reactions in many applications for solar energy conversion, photocatalysis, and optoelectronics. <sup>15-18</sup> Recent advances in ultrafast optical and X-ray spectroscopies have revealed that the CT excitation results in significant structural rearrangements, accompanied by CVWP motions associated with the structural changes in the vibronic manifold of the CT excited states. <sup>19-31</sup> Furthermore, the CVWP motions evolve along the excited state trajectories to the final states during intersystem crossing and spin-crossover dynamics, shedding light on the possibility of the vibronic coherence between different spin states. <sup>28, 29, 32-35</sup> These examples imply that the CVWP motions following the CT transition in the TMCs can exert a significant impact on subsequent PET toward the electron acceptor.

To investigate the effects of CVWP motion in PET reactions, we designed an electron donor-acceptor system (2) with a cyclometalated Pt(II) dimer (1) as the donor and naphthalene diimide (NDI) as the acceptor (Figure 1a). As shown in previous studies, a metal-metal-to-ligand charge transfer (MMLCT,  $d\sigma^* \to \pi^*$ ) transition in Pt(II) dimer directly induces ~ 0.2 Å or larger Pt-Pt distance contraction as the electron density from an antibonding orbital is depleted.<sup>28, 31, 36</sup> Meanwhile, a significant amplitude of CVWP motions associated with Pt-Pt stretching vibration can be launched in the MMLCT excited state, as evidenced by ultrafast optical transient absorption and X-ray solution scattering experiments.<sup>28, 31, 35</sup> In this study, using ultrafast broadband transient absorption (BBTA) spectroscopy with 20-fs (FWHM) pump pulses, we track the CVWP motions during the PET from Pt(II) dimer to NDI to identify the key reaction coordinates in 2. The results unveil the clear evidence for the certain CVWP motions to directly modulate the NDI radical anion formation dynamics and to influence the PET trajectories across the MMLCT and charge-separated (CS) states.

## **Results and Discussion**

Excited State and PET Kinetics. Pt(II) dimer (1) exhibits the typical electronic transitions of a cyclometalated Pt(II) dimer as reported in previous studies, featuring 1) ligand-centered (LC) transitions below 350 nm, 2) a mixture of LC and metal-to-ligand charge transfer (MLCT) transitions between 350 – 450 nm and 3) the MMLCT transition above 450 nm (Figure 1b, S5-7 and Table S1).36, 37 The electron donor-acceptor complex (2) also displays the MMLCT band above 450 nm, while a strong  $\pi$  -  $\pi$ \* transition of the NDI electron acceptors appears with a clear vibronic feature below 400 nm in the steady-state absorption spectrum (Figure 1b, S5-7 and Table S<sub>1</sub>),<sup>38</sup> We investigated the PET reaction dynamics from Pt(II) dimer to NDI upon MMLCT excitation using BBTA spectroscopy with 20-fs pump pulses centered at 550 nm (see the inset in Figure 1b). As a reference, the BBTA signals of 1 display rise dynamics across the entire probe spectral range within the first 2-3 picosecond (ps) time delay window (Figure 2a). After the first few ps, the TA signal amplitudes persist without significant changes up to 150 ps (Figure S8). Global fitting, performed with the Glotaran program<sup>39</sup> using a sequential kinetic model, reveals two time constants for the early rise kinetics: 364 fs and 1.76 ps. The analysis of evolutionassociated difference spectra (EADS) for each time component demonstrates that these rise kinetics are attributed to the decay kinetics of the stimulated emission (SE) signal (Figure 2c). The broad SE signal centered around 650 nm first emerges, which subsequently redshifts to 700 nm with a time constant of 364 fs and then is completely quenched with a time constant of 1.76 ps. Since the SE signal stems from the singlet MMLCT state, the time constant of 1.76 ps is

Chemical Science Page 6 of 48

attributed to intersystem crossing (ISC) from the singlet to the triplet MMLCT state. After undergoing vibrational cooling within 71 ps,<sup>37</sup> the <sup>3</sup>MMLCT state persists longer than 150 ps time window, which is consistent with the <sup>3</sup>MMLCT lifetime of 341 ns obtained from the previous nanosecond TA measurement on the same Pt(II) dimer<sup>36</sup>.

The BBTA signals of 2 exhibit distinctly different early TA kinetics (Figure 2b) under the same experimental conditions compared as those of 1. The formation of NDI radical anion dominates the temporal and spectral behaviors of 2 due to the PET from Pt(II) dimer to NDI. Using the global fitting of the sequential kinetic model, analysis of EADS demonstrates that the NDI anion spectrum rises with two time constants: 95 fs and 475 fs (Figure 2d). The black EADS corresponding to the 'MMLCT state converts to the red EADS with a 95 fs time constant, followed by the blue EADS with a 475 fs time constant. Notably, the red EADS differs significantly from the blue EADS and displays characteristic bands of NDI radical anion at 608, 700, and 775 nm.<sup>38</sup> Instead, the red EADS shows a broader absorption band at 608 nm and two blue-shifted bands at 667 and 750 nm. This distinction indicates that the charge separation (blue EADS) occurs through an intermediate CT (InCT) state formed between the Pt(II) dimer and NDIs (shown by the red EADS) following the MMLCT excitation. After the completion of the charge separation, the spectrum of the NDI anion decays over time without significant changes in its spectral features (Figure S8). The multiple time constants found in the decay kinetics (1.83, 15.1, and 220 ps) suggests that different relaxation processes could be present, such as vibrational relaxation or ISC during a charge recombination (CR) to the ground-state. Although a detailed investigation of these dynamics could provide insight into the mechanism of CR, the current study focuses on the forward PET processes (Pt(II) dimer  $\rightarrow$  NDI) which take place on a the time scale comparable to some vibrational motions and can be tracked by the CVWP behaviors to deduce their roles in the PET processes.

**CVWP Motions.** The CVWP motions in both **1** and **2** launched by the **20**-fs pump pulses were detected as oscillatory signals across the probe range overlaid with the population evolution signals (Figures 3a and 3b). Fast Fourier transformation (FFT) of the beating signals after the removing the population evolution in the TA signal uncovers the frequencies of the CVWP motions for **1** and **2** below 1000 cm<sup>-1</sup>, as shown in Figures 3c and 3d. (Note: the THF solvent vibration at 912 cm<sup>-1</sup> is induced by an impulsive stimulated Raman scattering (ISRS) process<sup>40</sup>). Previous ultrafast TA studies on cyclometalated Pt(II) dimers, combined with normal mode analysis, showed a frequency upshift in the CVWP motion associated with the Pt-Pt stretching vibration from ~ 110 cm<sup>-1</sup> for the ground-state to ~ 150 cm<sup>-1</sup> for the MMLCT excited-state as the

result of the Pt-Pt distance shortening or effective bond order increase.<sup>28, 29, 35</sup> Particularly, fs X-ray solution scattering study directly observed a contraction of Pt-Pt distance by ~0.2 Å in the MMLCT excited-state, accompanied by the Pt-Pt stretching motion with the 150 cm<sup>-1</sup> frequency.<sup>31</sup> In the current investigation, the CVWPs of 1 and 2 also exhibit significant FFT amplitudes at ~110 and ~150 cm<sup>-1</sup> (Figure 3c and d), which are similar to the aforementioned frequencies of Pt-Pt stretching vibrations in the ground- and MMLCT excited-states, respectively.

Our fs-BBTA spectroscopy provides a broad probe spectral range of 550 - 850 nm, allowing us to precisely map out a phase-flip position associated with the Pt-Pt stretching CVWP motion and its temporal evolution (black dotted arrows in Figures 3a and 3b). Since the phase flip occurs around the energy minimum of the potential energy surface (PES), its spectral position provides the assignments of the electronic state where the CVWP motions take place.<sup>29, 41-45</sup> Specifically, the phase flip in the ground-state CVWP would occur around the ground-state bleaching (GSB) maximum, while that in the excited-state CVWP arises near the SE or excited-state absorption (ESA) maximum.

In Figure 3a, the wavelength-resolved residual map for 1 reveal that the phase flip emerges first around 650 nm and then redshifts to ~ 700 nm, which is consistent with the redshift of the SE maximum from 650 to 700 nm with the time constant of 364 fs (Figure 2c). The temporal evolution of the phase flip demonstrates that the 150 cm<sup>-1</sup> CVWP motion directly modulates the SE spectral shape and amplitude along the probe wavelength axis (also see Figure S10). In addition, the CVWP undergoes a damping with a time constant of ~ 610 fs (Figure S11 and Table S2). These results confirm that the 150 cm<sup>-1</sup> Pt-Pt stretching CVWP launched by the <sup>1</sup>MMLCT excitation decays in the PES of the 'MMLCT excited state during the ISC to the 'MMLCT state. In contrast, the phase flip for the 150 cm<sup>-1</sup> CVWP motions in 2 disappears at the SE peak of 650 nm in < 300 fs, while a new phase flip emerges at 800 nm in early time and blueshifts to 750 nm. Moreover, the 150 cm<sup>-1</sup> CVWP motions of 2 display an initial amplitude growth within ~100 fs, similar to the TA rise time of ~100 fs associated with forming the InCT state in the PET process (Figure S11 and Table S2). These features differentiate the origin of the 150 cm<sup>-1</sup> CVWPs for 2 from that for 1. The decay and rise of the phase flip at  $\sim 650$  and  $\sim 800$  nm demonstrate that the PET reaction quenches the SE signal of the ¹MMLCT excited-state and concomitantly enhances the ESA signals of the InCT and CS states. In addition, the damping time of ~ 1 ps indicates that the Pt-Pt stretching CVWP sustains its phase during the PET reaction (Figure S11 and Table S2).

Chemical Science Page 8 of 48

Therefore, the 150 cm<sup>-1</sup> CVWP motion observed in **2** is attributed to the nuclear motion associated with the Pt-Pt stretching vibration in the InCT and CS states.

In Figures 3c and d, FFT analysis also reveals other CVWP motions in 200 – 700 cm<sup>-1</sup> frequency range. The weak FFT amplitudes were observed at 230 and 293 cm<sup>-1</sup> in 1, which were not clearly detected in previous work.<sup>28</sup> The 230 and 293 cm<sup>-1</sup> modes largely appear beyond the onset of the absorption spectra at ~ 600 nm and thus can be reasonably assigned to the CVWPs in the <sup>1</sup>MMLCT excited-state. The 230 cm<sup>-1</sup> CVWP motion is also observed in 2, while its spectral amplitude distribution is distinct. The mode is predominantly detected around 608 and 667 nm, which are near the peaks of InCT state represented by red EADS (Figure 2d). 2 also shows new CVWP motions with the frequencies of 270, 308, 345, 540 and 678 cm<sup>-1</sup> around 608 nm peak of NDI anion. Interestingly, the wavelength-resolved residual map displays the beating patterns of these modes (dominantly 678 cm<sup>-1</sup> frequency) with the phase flip around 608 nm (black dotted arrow in Figure 3b). Additionally, the amplitude of the 678 cm<sup>-1</sup> beating signal gradually increases over a period of ~ 0.8 ps, as shown in the oscillation at 615nm (Figure 3b).

Franck-Condon vs. Herzberg-Teller Type CVWP Oscillations. The FFT amplitude spectra plotted as a function of probe wavelength provide further characterization of the CVWP motions in 2 (Figure 4a and S12). The FFT amplitude of the 678 cm<sup>-1</sup> mode is predominantly present around the NDI radical anion band at 608 nm. Similar behavior is observed in the FFT amplitudes of 270, 308, 345, and 540 cm<sup>-1</sup> CVWPs (Figure S12). The spectra show a distinct valley at 608 nm due to the phase flip of the CVWP motion, which is consistent with the wavelength resolved residual map (black dotted arrow at 608 nm in Figure 3b). These CVWP motions are attributed to Franck-Condon type oscillations. As illustrated in Figure 4b, the periodic propagation of the CVWP motions along its vibrational coordinates leads to spectral modulations of the NDI radical anion due to the displacement between the PESs of the lowest (S1) and higher excited states (Sn) in the ESA region. Specifically, the 678 cm<sup>-1</sup> CVWP motion causes the peak of NDI radical anion band to oscillate between wavelengths larger (~615 nm) and smaller (~595 nm) than 608 nm with its vibrational frequency. Although we do not directly excite NDI, the phase flip at the peak of the NDI radical anion absorption strongly indicates that the CVWPs in 2 originates from the nuclear motions associated with the CS active vibration pertaining to the NDI core.46 However, the PET time scales of ~ 100 and ~500 fs are not sufficiently short to impulsively generate 50 fs period of 678 cm<sup>-1</sup> CVWP mode. This result suggests a different mechanism for the formation of 678 cm<sup>-1</sup> CVWP motion in the CS state of 2.

The FFT amplitude for the 230 cm<sup>-1</sup> CVWP displays two bands with peaks around 608 and 667 nm. Importantly, these peaks match well with the characteristic bands at 608 and 667 nm of the red EADS corresponding to the InCT state of the PET reaction (Figure 4a). This feature indicates that the 230 cm<sup>-1</sup> CVWP motion only modulates the amplitudes of both ~608 and 667 nm bands without the spectral shifts, in contrast to the 678 cm<sup>-1</sup> motion. Such CVWP motions can be interpreted as Herzberg-Teller type oscillation, as illustrated in Figure 4b.<sup>47-50</sup> In this case, the CVWP motion cannot modulate the TA spectral shape and amplitude because the displacement between the two PESs is negligible or zero; therefore, the transition energies on both sides of the PES are identical. When the nuclear motions, however, can differentiate the oscillator strength on the right and left sides of the PES, it can be possible to probe the intensity modulation while maintaining the spectral shape. This feature is the evidence for strong vibronic coupling, referred to as the non-Condon effect reported in the CVWP dynamics of several molecular systems, 47-50 The observation of the non-Condon effect at 230 cm<sup>-1</sup> in 2 also suggests that this CVWP motion alters the transition strengths of the electronic transitions at ~ 608 and 667 nm. Given that these transition strengths are proportional to the population of the InCT state in the PET processes, the 230 cm<sup>-1</sup> nuclear motion is vibronically coupled to the PET reaction, directly modulating the population of the InCT state from the ¹MMLCT state.

The Pt-Pt stretching vibration (150 cm<sup>-1</sup> mode) exhibits FFT amplitude spectra characterized by a sharp peak at ~ 608 nm and a broad peak at ~ 700 nm (Figure 4a). These features match the NDI anion bands in the CS state (blue EADS in Figure 2d). Notably, the oscillation residual map reveals the absence of phase flips associated with the 150 cm<sup>-1</sup> oscillation at ~ 608 nm and ~ 700 nm (Figure 3b). The presence of a phase flip near 750 nm (black dotted arrow in Figure 3b and red arrow in Figure 4a) complicates the assignment of the origin of the 150 cm<sup>-1</sup> CVWP. Nevertheless, the FFT spectral features at ~608 and 700 nm strongly suggests the non-Condon effect in the 150 cm<sup>-1</sup> vibration, leading to alternation in the intensity of the NDI radical anion spectrum. In other words, the result indicates that the Pt-Pt stretching motion is vibronically coupled to the PET reaction, specifically related to the formation of the CS state from the InCT state.

**Solvent-Polarity Dependence of PET and CVWP Dynamics.** To verify the correlations of the PET kinetics and the CVWP evolution, we also investigated the solvent dependence of the PET and CVWP dynamics (Figure S13-14). It is well-known from Marcus theory that the solvent reorganization energy in the ET processes changes with its dielectric constant, and thus the PET rate.<sup>51</sup> Generally, the polar solvent stabilizes the charged species (radical cations and anions, i.e.,

Chemical Science Page 10 of 48

CS state) and thus increases the driving force of the PET reaction. We anticipated that a polar solvent would enhance the PET rate and affect the damping or rise time of the CVWP motions. This approach allows us to identify the CVWP motions associated with the PET reaction coordinates.<sup>52-54</sup> As shown in Figure 5b, the rise kinetics of NDI anion peak at  $\sim$  608 nm become faster as the polarity increases; toluene (dielectric constant  $\varepsilon \approx 2.38$ ) < THF ( $\varepsilon \approx 7.58$ ) < acetonitrile (MeCN,  $\varepsilon \approx 37.5$ ). The global kinetic analysis further reveals the solvent polarity dependency of the PET processes (Figure 2d and 5a): 1) the time scale of  $\sim$  100 fs corresponding to the formation of the InCT state (the red EADS) remain almost unchanged across different solvent polarities. 2) the transition from the InCT to the CS state (the blue EADS) becomes faster with increasing polarity, toluene (952 fs) > THF (475 fs) > MeCN (224 fs). 3) the CR processes also occur faster in higher polarity solvents.

Using the short-time Fourier transformation (STFT) method, we analyze the temporal evolution of the CVWP motions and their correlation with the PET kinetics observed in different solvents (Figure 5c, S16 and S17). The STFT analysis captures the time evolution of the amplitude of the frequency content extracted from the oscillatory signals (see the details in Figure S15). The amplitude of the 230 cm<sup>-1</sup> mode decreases almost completely within 0.6 ps, and its dephasing dynamics appear to be independent of solvent polarity. The 150 cm<sup>-1</sup> mode exhibits a noticeable dependence on solvent polarity. The time point at which the amplitude reaches half of its maximum value becomes smaller with increasing solvent polarity, ranging from ~ 0.9 ps in toluene, ~0.6 ps in THF to ~0.4 ps in MeCN. This trend illustrates that the 150 cm<sup>-1</sup> CVWP undergoes faster dephasing dynamics in higher polar solvents. Most interestingly, the 678 cm<sup>-1</sup> CVWP clearly show a distinct trend from the others, with its amplitude rise during the PET processes. As the solvent polarity increases, the STFT amplitude reaches its maximum faster at earlier delay times, ~0.8 ps in THF to ~0.6 ps in MeCN. The onset of the amplitude decay for the 678 cm<sup>-1</sup> mode also varies with the solvent polarity, which can be interpreted as the consequence of the polar solvents accelerating both CS and CR processes. This finding demonstrates that the rise dynamics of this mode become faster as the polarity increases, which is consistent with the faster rise of NDI anion in MeCN solvent (Figure 5b). Although the STFT amplitude at eraly time is the lowest in toluene, the time point at the maximum value remains similar to THF, followed by slower dephasing. This result indicates that the 678 cm<sup>-1</sup> CVWP in toluene begins the damping concurrently with the rise dynamics during the PET processes, distinct from those observed in other solvents. The 270, 308, 345 and 540 cm<sup>-1</sup> CVWPs do not show the polarity dependence (Figure S17).

The observation of the non-Condon effect for the 230 and 150 cm<sup>-1</sup> CVWPs evidences its strong vibronic coupling with the PET processes,  ${}^{1}MMLCT \rightarrow InCT \rightarrow CS$  (Figure 4). The solventpolarity dependence of the PET and CVWP dynamics further confirms this assignment. The absence of polarity dependence in the 230 cm<sup>-1</sup> CVWP dynamics supports that the nuclear motion is coupled to the initial PET coordinate for the transition from the MMLCT to InCT state before the solvent reorganization occurs. In contrast, the 150 cm<sup>-1</sup> CVWP dynamics follow a similar trend to the TA kinetics of the InCT state (the red EADS in Figure 2d and 5a), which varies with solvent polarity. This result suggests that the Pt-Pt stretching vibration emerges as the key coordinate coupled with the subsequent PET reaction from the InCT to CS state. Compared to the damping dynamics of 230 and 150 cm<sup>-1</sup> CVWPs, the 678 cm<sup>-1</sup> CVWP dynamics clearly exhibit an intensity growth during the PET processes. Since the amplitude rise dynamics depend on the PET rate varied by solvent polarity, we rule out the possibility that this CVWP is a spectator mode orthogonal to the PET reaction coordinate and, thus, not active in the reaction. As mentioned in the previous section, the impulsive generation via the PET processes is also excluded because the PET time scales of ~ 100 and 224 - 950 fs are much longer than the vibrational period of 678 cm<sup>-1</sup> CVWP (~50fs). Hence, the 678 cm<sup>-1</sup> CVWP transfer strongly suggests the vibronic mechanism for the entire PET processes,  ${}^{1}MMLCT \rightarrow InCT \rightarrow CS$ , which will be discussed below.

**Key PET Reaction Coordinates.** To gain insight into how the molecular vibrations of 150, 230, and 678 cm<sup>-1</sup> modes contribute to the PET reactions, we conducted calculations involving optimized structures and normal modes in both ground- and CS states (Figure 6a and S18-23). Based on the knowledge of which the 150 cm<sup>-1</sup> CVWP motion originates from the Pt-Pt stretching vibration, our initial focus is on examining the relevant normal modes in the ground- and CS states. Similar to **1**, the Pt-Pt stretching vibration in **2** exhibits an upshift in frequency from 113 cm<sup>-1</sup> in the ground- to 148 cm<sup>-1</sup> in CS state. It is because the one electron transferred to the NDI comes from a dσ\* antibonding orbital, leading to Pt-Pt bond contraction. Notably, the nuclear motion triggers an out-of-plane (OOP) motion of 2-phenylpyridine (ppy) ligands (left in Figures 6a and S19), which arises due to the short distance (~ 3.6 Å) between these ligands. More interestingly, the induced OOP motion concurrently leads to a dihedral angle (DA) change between the ppy ligand and the NDI moiety, resulting in ~ 5° alteration (Figure S21). The DA alteration can potentially increase the overlap of  $\pi$  orbitals between the ppy and NDI, thereby accelerating the transfer of electrons from ppy to NDI. Such a torsional motion has been noted

Chemical Science Page 12 of 48

to enhance  $\pi$ -interactions, leading to rapid intramolecular CT in copolymers and covalent organic frameworks built from donor-bridge-acceptor configurations.<sup>55-57</sup>

Based on the Pt-Pt stretching motion, we searched for an OOP vibration within the 200 – 300 cm<sup>-1</sup> frequency range, potentially corresponding to the 230 cm<sup>-1</sup> mode. The calculated OOP vibrational mode has a frequency around 282 cm<sup>-1</sup> in both the ground- and CS states, displaying an alteration of the DA by ~ 5° (middle in Figure 6a and Figures S19 and S22). The OOP motion is also observable around a similar frequency in the normal mode analysis for 1 (Figure S20), consistent with the CVWP motion observation at ~ 230 cm<sup>-1</sup> in 1 and 2 (Figure 3c and d). An intriguing collective vibration involving both the ppy ligand and NDI core was calculated around 687 cm<sup>-1</sup> in both ground and CS states (right in Figure 6a). This nuclear motion alters ~ 0.06 Å in the bond distance between the ppy and NDI constituents (Figure S23). Therefore, the molecular vibrations of 150, 230 and 678 cm<sup>-1</sup> frequencies are expected to be PET active due to the alternation of DA and bond length between the ppy and NDI moieties.

Based on the analyses of CVWP motions and their corresponding normal modes, the PET reaction mechanism for 2 can be proposed, as illustrated in Figure 6b. In the initial PET process (~ 100 fs), the 'MMLCT and InCT states are vibronically coupled via the 230 cm<sup>-1</sup> OOP vibration initiated by the MMLCT excitation. This vibration leads to an enhancement in  $\pi$ -interaction between the ppy and NDI moieties through the modulation in the DA configuration. Even though the 230 cm<sup>-1</sup> mode completely decoheres in the InCT state, the  $\pi$ -interaction keeps being boosted through the vibration of the Pt-Pt stretching mode (150 cm<sup>-1</sup>), which also alters in the DA configuration. Consequently, the vibronic couplings driven by the OOP and Pt-Pt stretching vibrations render the efficient PET pathway through the multiple PESs. More importantly, the PET pathway is accompanied by coherence transfer of the 678 cm<sup>-1</sup> CVWP to the CS state. The DA modulations enable vibronic wavefunction delocalization across the multiple PESs, leading to the transfer of the 678 cm<sup>-1</sup> CVWP along the entire PET processes. Along this line, the vibronic couplings driven by the OOP and Pt-Pt stretching vibrations may engender multiple conical intersections (CIs) through the PET trajectories (Figure 6b). The CI is a crossing region where two adiabatic PESs are degenerate at a particular geometry. In this vicinity, strong vibronic mixing of the electronic and nuclear degrees of freedom dominates, leading to the breakdown of the Born-Oppenheimer approximation and enabling nonadiabatic transitions from the higher to lower surfaces.<sup>58-60</sup> Such vibronic coupling significantly influences the CVWP dynamics at the CI, facilitating its passage through the CI and subsequent population in the final state. 61, 62 In 2, the DA modulations enhance the nonadiabatic couplings at the CIs, conserving

the 678 cm<sup>-1</sup> wavepacket phase and leading to efficient coherence transfer to the CS state. In other words, the 678 cm<sup>-1</sup> CVWP in **2** passes through the two CIs in the crossing regions between the PESs of the MMLCT, InCT and CS states, followed by dephasing processes during the CR processes. In this context, it is conceivable that the InCT state represents a vibronic CT state delocalized between the ppy and NDI, vibronically bridging the <sup>1</sup>MMLCT and CS states during the PET processes. The strong dependence of the TA kinetics for the InCT state on the solvent polarity also supports this interpretation. Furthermore, the calculated collective motion involving the ppy and NDI entities may signify a distinct intramolecular vibration associated with the vibronic CT.

Conclusions. In summary, we experimentally detected that MMLCT excitation of Pt(II) dimer launches certain CVWP motions (150, 230 and 678 cm<sup>-1</sup>) which directly alter the formation and evolution of the NDI radical anion during PET. The temporal correlation between the CVWP and the PET dynamics revealed these modes as key reaction coordinates for the PET processes. Based on normal mode analysis, these findings strongly suggest that the CVWP motions are coupled to the PET reaction coordinates by modulating the energies associated with vibronic states to be delocalized between the ligand and NDI. As a result, we also discovered the dynamic interplay of these vibronic motions enables the 678 cm<sup>-1</sup> vibronic coherence to survive the entire PET processes, even in ~ 1 ps CS in toluene. Our findings demonstrate new possibility to leverage the vibronic effect to determine the most desirable trajectory for an efficient PET reaction. The vibrational motions coupled to the CT transition of TMCs will offer an ideal avenue for harnessing the vibration-assisted coherent ET in artificial solar energy conversion systems.

### **Conflicts of Interest**

There are no conflicts to declare.

# Acknowledgements

P.K., S.R., A.J.S.V, X.L., S.K., T.W.K., X.L., F.N.C and L.X.C. as well as computational work are supported in part by the Ultrafast Initiative of the U. S. Department of Energy, Office of Science, Office of Basic Energy Sciences, through Argonne National Laboratory under Contract No. DE-AC02-06CH11357. The development of computational method for simulating excited state

Chemical Science Page 14 of 48

dynamics is supported by the National Science Foundation (CHE-1856210 to X.L). The synthesis and initial spectroscopic characterization were supported by the National Science Foundation (CHE-2247821 to L.X.C and CHE-2247822 to F.N.C).

### **References**

- 1. G. R. Fleming and R. v. Grondelle, *Physics Today*, 1994, **47**, 48-55.
- 2. M. H. Vos, F. Rappaport, J.-C. Lambry, J. Breton and J.-L. Martin, *Nature*, 1993, **363**, 320-325.
- 3. K. Ando and H. Sumi, *The Journal of Physical Chemistry B*, 1998, **102**, 10991-11000.
- 4. V. I. Novoderezhkin, A. G. Yakovlev, R. van Grondelle and V. A. Shuvalov, *The Journal of Physical Chemistry B*, 2004, **108**, 7445-7457.
- 5. E. Romero, R. Augulis, V. I. Novoderezhkin, M. Ferretti, J. Thieme, D. Zigmantas and R. van Grondelle, *Nature Physics*, 2014, **10**, 676-682.
- 6. F. D. Fuller, J. Pan, A. Gelzinis, V. Butkus, S. S. Senlik, D. E. Wilcox, C. F. Yocum, L. Valkunas, D. Abramavicius and J. P. Ogilvie, *Nature Chemistry*, 2014, **6**, 706-711.
- 7. F. Ma, E. Romero, M. R. Jones, V. I. Novoderezhkin and R. van Grondelle, *The Journal of Physical Chemistry Letters*, 2018, **9**, 1827-1832.
- 8. V. I. Novoderezhkin, E. Romero and R. van Grondelle, *Physical Chemistry Chemical Physics*, 2015, **17**, 30828-30841.
- 9. E. Romero, V. I. Novoderezhkin and R. van Grondelle, Nature, 2017, 543, 355-365.
- 10. J.-L. Brédas, E. H. Sargent and G. D. Scholes, Nature Materials, 2017, 16, 35-44.
- 11. G. D. Scholes, G. R. Fleming, L. X. Chen, A. Aspuru-Guzik, A. Buchleitner, D. F. Coker, G. S. Engel, R. van Grondelle, A. Ishizaki, D. M. Jonas, J. S. Lundeen, J. K. McCusker, S. Mukamel, J. P. Ogilvie, A. Olaya-Castro, M. A. Ratner, F. C. Spano, K. B. Whaley and X. Zhu, *Nature*, 2017, **543**, 647-656.
- 12. S. Rafig and G. D. Scholes, *Journal of the American Chemical Society*, 2019, **141**, 708-722.
- 13. S. M. Falke, C. A. Rozzi, D. Brida, M. Maiuri, M. Amato, E. Sommer, A. De Sio, A. Rubio, G. Cerullo, E. Molinari and C. Lienau, *Science*, 2014, **344**, 1001-1005.
- 14. Q. Bian, F. Ma, S. Chen, Q. Wei, X. Su, I. A. Buyanova, W. M. Chen, C. S. Ponseca, M. Linares, K. J. Karki, A. Yartsev and O. Inganäs, *Nature Communications*, 2020, **11**, 617.
- 15. D. M. Schultz and T. P. Yoon, *Science*, 2014, **343**, 1239176.
- 16. O. S. Wenger, *Journal of the American Chemical Society*, 2018, **140**, 13522-13533.
- 17. J. Twilton, C. Le, P. Zhang, M. H. Shaw, R. W. Evans and D. W. C. MacMillan, *Nature Reviews Chemistry*, 2017, **1**, 0052.
- 18. V. W.-W. Yam, V. K.-M. Au and S. Y.-L. Leung, *Chemical Reviews*, 2015, **115**, 7589-7728.
- 19. M. Iwamura, S. Takeuchi and T. Tahara, Acc. Chem. Res., 2015, 48, 782-791.
- 20. T. Katayama, T. Northey, W. Gawelda, C. J. Milne, G. Vankó, F. A. Lima, R. Bohinc, Z. Németh, S. Nozawa, T. Sato, D. Khakhulin, J. Szlachetko, T. Togashi, S. Owada, S.-i. Adachi, C. Bressler, M. Yabashi and T. J. Penfold, *Nature Communications*, 2019, **10**, 3606.
- 21. G. Auböck and M. Chergui, *Nature Chemistry*, 2015, **7**, 629-633.
- 22. F. Hainer, N. Alagna, A. Reddy Marri, T. J. Penfold, P. C. Gros, S. Haacke and T. Buckup, *The Journal of Physical Chemistry Letters*, 2021, **12**, 8560-8565.
- 23. H. T. Lemke, K. S. Kjær, R. Hartsock, T. B. van Driel, M. Chollet, J. M. Glownia, S. Song, D. Zhu, E. Pace, S. F. Matar, M. M. Nielsen, M. Benfatto, K. J. Gaffney, E. Collet and M. Cammarata, *Nature Communications*, 2017, **8**, 15342.
- 24. K. Kunnus, M. Vacher, T. C. B. Harlang, K. S. Kjær, K. Haldrup, E. Biasin, T. B. van Driel, M. Pápai, P. Chabera, Y. Liu, H. Tatsuno, C. Timm, E. Källman, M. Delcey, R. W. Hartsock, M. E. Reinhard, S.

- Koroidov, M. G. Laursen, F. B. Hansen, P. Vester, M. Christensen, L. Sandberg, Z. Németh, D. S. Szemes, É. Bajnóczi, R. Alonso-Mori, J. M. Glownia, S. Nelson, M. Sikorski, D. Sokaras, H. T. Lemke, S. E. Canton, K. B. Møller, M. M. Nielsen, G. Vankó, K. Wärnmark, V. Sundström, P. Persson, M. Lundberg, J. Uhlig and K. J. Gaffney, *Nature Communications*, 2020, **11**, 634.
- 25. S. Cho, M. W. Mara, X. Wang, J. V. Lockard, A. A. Rachford, F. N. Castellano and L. X. Chen, *The Journal of Physical Chemistry A*, 2011, **115**, 3990-3996.
- 26. P. Kim, M. S. Kelley, A. Chakraborty, N. L. Wong, R. P. Van Duyne, G. C. Schatz, F. N. Castellano and L. X. Chen, *The Journal of Physical Chemistry C*, 2018, **122**, 14195-14204.
- 27. L. Mewes, R. A. Ingle, S. Megow, H. Böhnke, E. Baranoff, F. Temps and M. Chergui, *Inorganic Chemistry*, 2020, **59**, 14643-14653.
- 28. P. Kim, A. J. S. Valentine, S. Roy, A. W. Mills, A. Chakraborty, F. N. Castellano, X. Li and L. X. Chen, *The Journal of Physical Chemistry Letters*, 2021, **12**, 6794-6803.
- 29. P. Kim, A. J. S. Valentine, S. Roy, Alexis W. Mills, F. N. Castellano, X. Li and L. X. Chen, *Faraday Discussions*, 2022, **237**, 259-273.
- 30. T. W. Kim, P. Kim, A. W. Mills, A. Chakraborty, S. Kromer, A. J. S. Valentine, F. N. Castellano, X. Li and L. X. Chen, *The Journal of Physical Chemistry C*, 2022, **126**, 11487-11497.
- 31. D. Leshchev, A. J. S. Valentine, P. Kim, A. W. Mills, S. Roy, A. Chakraborty, E. Biasin, K. Haldrup, D. J. Hsu, M. S. Kirschner, D. Rimmerman, M. Chollet, J. M. Glownia, T. B. van Driel, F. N. Castellano, X. Li and L. X. Chen, *Angewandte Chemie International Edition*, 2023, **62**, e202304615.
- 32. B. C. Paulus, S. L. Adelman, Lindsey L. Jamula and James K. McCusker, *Nature*, 2020, **582**, 214-218.
- 33. J. D. Gaynor, J. Sandwisch and M. Khalil, *Nature Communications*, 2019, **10**, 5621.
- 34. R. Monni, G. Capano, G. Auböck, H. B. Gray, A. Vlček, I. Tavernelli and M. Chergui, *Proceedings of the National Academy of Sciences*, 2018, **115**, E6396.
- 35. S. Rafiq, N. P. Weingartz, S. Kromer, F. N. Castellano and L. X. Chen, *Nature*, 2023, DOI: 10.1038/s41586-023-06233-y.
- 36. A. Chakraborty, J. E. Yarnell, R. D. Sommer, S. Roy and F. N. Castellano, *Inorganic Chemistry*, 2018, **57**, 1298-1310.
- 37. S. E. Brown-Xu, M. S. J. Kelley, K. A. Fransted, A. Chakraborty, G. C. Schatz, F. N. Castellano and L. X. Chen, *The Journal of Physical Chemistry A*, 2016, **120**, 543-550.
- 38. S. V. Bhosale, C. H. Jani and S. J. Langford, *Chemical Society Reviews*, 2008, **37**, 331-342.
- 39. J. J. Snellenburg, S. P. Laptenok, R. Seger, K. M. Mullen and I. H. M. van Stokkum, *J Stat Softw*, 2012, **49**, 1-22.
- 40. L. Dhar, J. A. Rogers and K. A. Nelson, *Chemical Reviews*, 1994, **94**, 157-193.
- 41. S. D. McClure, D. B. Turner, P. C. Arpin, T. Mirkovic and G. D. Scholes, *The Journal of Physical Chemistry B*, 2014, **118**, 1296-1308.
- 42. S. Rafiq and G. D. Scholes, *The Journal of Physical Chemistry A*, 2016, **120**, 6792-6799.
- 43. R. Xian, G. Corthey, D. M. Rogers, C. A. Morrison, V. I. Prokhorenko, S. A. Hayes and R. J. D. Miller, *Nature Chemistry*, 2017, **9**, 516-522.
- 44. C. Fitzpatrick, J. H. Odhner and R. J. Levis, *The Journal of Physical Chemistry A*, 2020, **124**, 6856-6866.
- 45. V. K. Jaiswal, P. Kabaciński, B. E. Nogueira de Faria, M. Gentile, A. M. de Paula, R. Borrego-Varillas, A. Nenov, I. Conti, G. Cerullo and M. Garavelli, *Journal of the American Chemical Society*, 2022, **144**, 12884-12892.
- 46. A. Aster, A.-B. Bornhof, N. Sakai, S. Matile and E. Vauthey, *The Journal of Physical Chemistry Letters*, 2021, **12**, 1052-1057.
- 47. H. Kano, T. Saito and T. Kobayashi, *The Journal of Physical Chemistry A*, 2002, **106**, 3445-3453.

Chemical Science Page 16 of 48

- 48. Y. Yoneda, H. Sotome, R. Mathew, Y. A. Lakshmanna and H. Miyasaka, *The Journal of Physical Chemistry A*, 2020, **124**, 265-271.
- 49. H. Kuramochi, G. Aoyama, H. Okajima, A. Sakamoto, S. Kanegawa, O. Sato, S. Takeuchi and T. Tahara, *Angewandte Chemie International Edition*, 2020, **59**, 15865-15869.
- 50. S. H. Sohn, W. Heo, C. Lee, J. Kim and T. Joo, *The Journal of Physical Chemistry A*, 2019, **123**, 6904-6910.
- 51. R. A. Marcus and N. Sutin, *Biochimica et Biophysica Acta (BBA) Reviews on Bioenergetics*, 1985, **811**, 265-322.
- 52. S. Rafiq, B. Fu, B. Kudisch and G. D. Scholes, *Nature Chemistry*, 2021, **13**, 70-76.
- 53. Y. Yoneda, B. Kudisch, S. Rafiq, M. Maiuri, Y. Nagasawa, G. D. Scholes and H. Miyasaka, *Journal of the American Chemical Society*, 2021, **143**, 14511-14522.
- 54. S. Rafiq and G. D. Scholes, *Chemical Physics Letters*, 2017, **683**, 500-506.
- 55. I. Hwang, S. Beaupré, M. Leclerc and G. D. Scholes, *Chemical Science*, 2012, **3**, 2270-2277.
- 56. P. Roy, A. Jha, V. B. Yasarapudi, T. Ram, B. Puttaraju, S. Patil and J. Dasgupta, *Nature Communications*, 2017, **8**, 1716.
- 57. T. W. Kim, S. Jun, Y. Ha, R. K. Yadav, A. Kumar, C.-Y. Yoo, I. Oh, H.-K. Lim, J. W. Shin, R. Ryoo, H. Kim, J. Kim, J.-O. Baeg and H. Ihee, *Nature Communications*, 2019, **10**, 1873.
- 58. G. A. Worth and L. S. Cederbaum, *Annual Review of Physical Chemistry*, 2004, **55**, 127-158.
- 59. W. Domcke and D. R. Yarkony, *Annual Review of Physical Chemistry*, 2012, **63**, 325-352.
- 60. Y. Boeije and M. Olivucci, *Chemical Society Reviews*, 2023, **52**, 2643-2687.
- 61. A. Kühl and W. Domcke, *The Journal of Chemical Physics*, 2002, **116**, 263-274.
- D. Egorova and W. Domcke, *Journal of Photochemistry and Photobiology A: Chemistry*, 2004, **166**, 19-31.

Page 17 of 48 Chemical Science

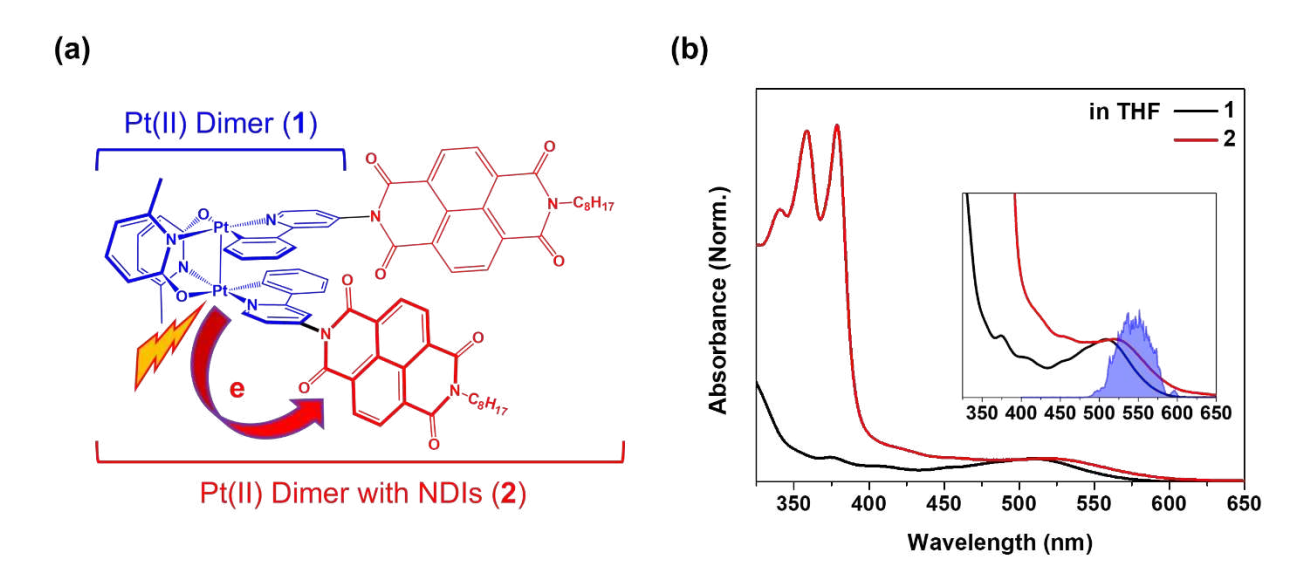


**Figure 1.** (a) Schematic molecular structures of Pt(II) dimer (1) as the donor and Pt(II) dimer with NDIs (2) as the donor-acceptor complex. (b) steady-state absorption spectra for 1 and 2 dissolved in THF solvent. The inset shows a zoom of MMLCT absorption bands and pump spectrum used in the BBTA measurements.

Chemical Science Page 18 of 48

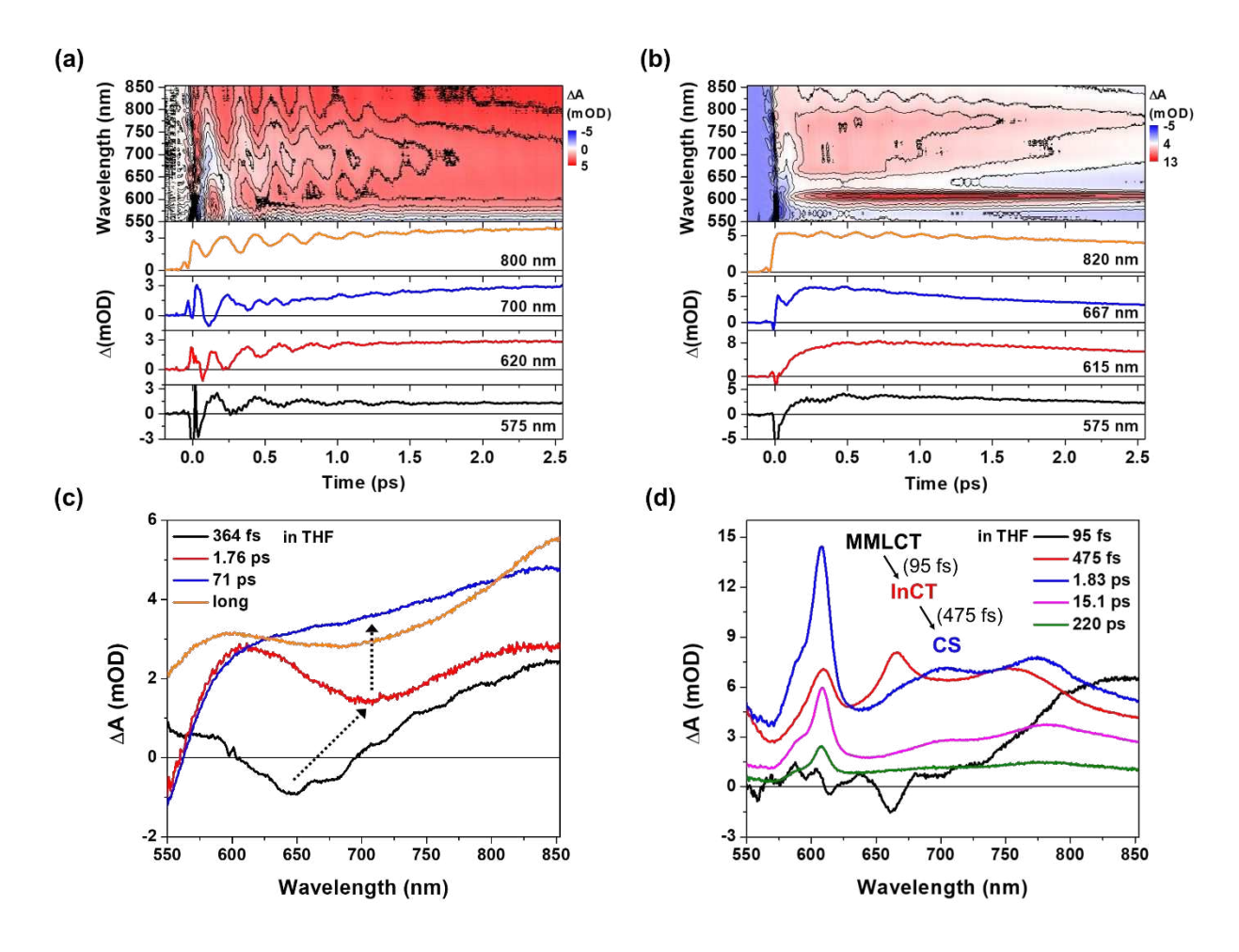


**Figure 2.** (a and b) 2D contour plots of BBTA spectra and kinetic profiles at specific probe wavelengths for **1** (a) and **2** (b). All measurements were carried out in THF solvent. (c and d) evolution associated difference spectra (EADS) for **1** (c) and **2** (d), obtained by global kinetic analysis on the BBTA data scanned up to 150 ps (Figure S8). Black arrows highlight the temporal evolution of stimulated emission (SE) signal. The BBTA data up to 70 fs were truncated for the global fitting in order to avoid the contribution of coherent spike and crossphase modulation signal around time zero.

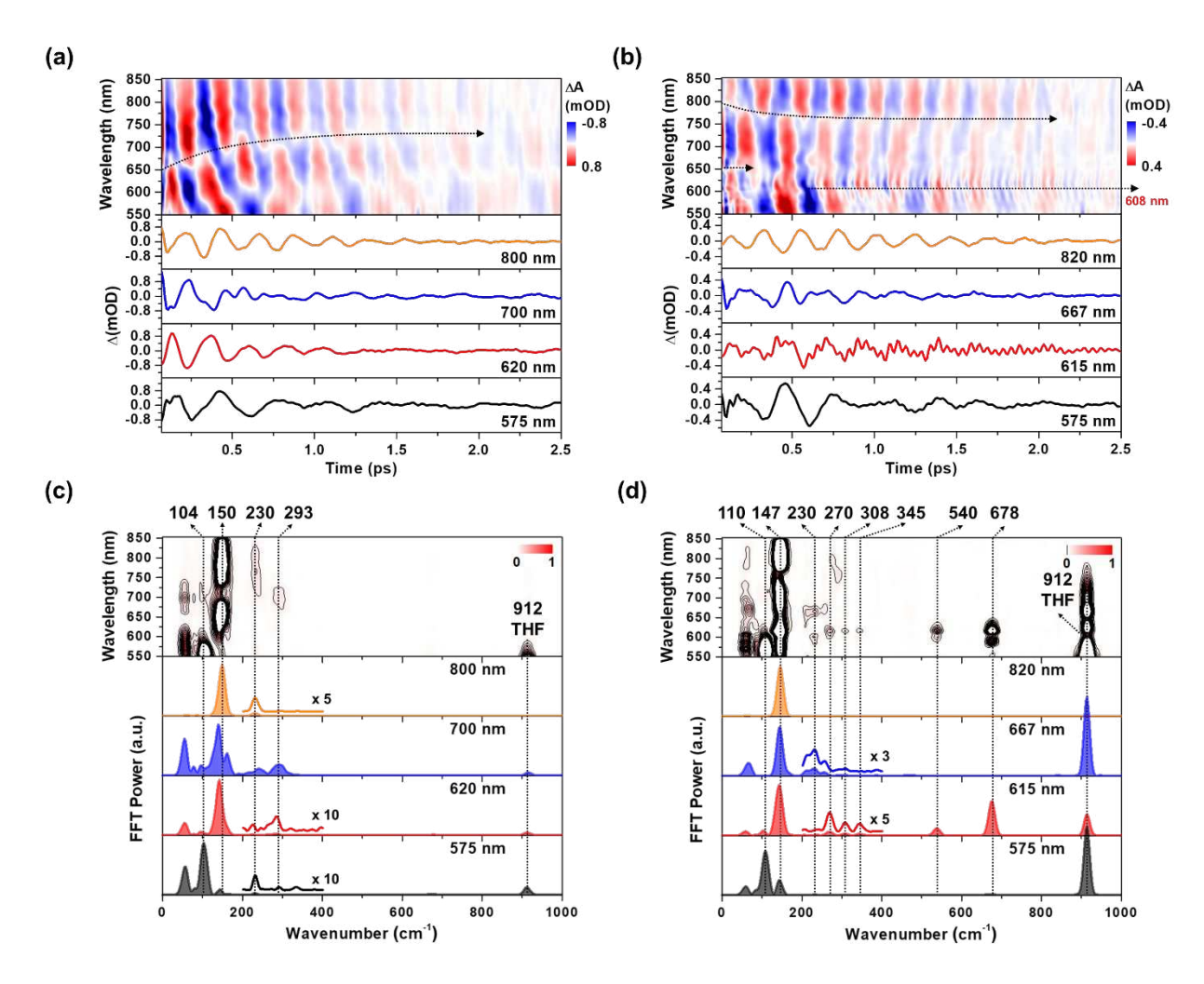


**Figure 3.** (a and b) wavelength-resolved residual map (top) and beating signals (bottom) at specific wavelengths for  $\bf 1$  (a) and  $\bf 2$  (b). The oscillatory residuals were extracted by a global kinetic analysis on the BBTA kinetic traces. We performed inverse Fourier filtering on the CVWP modes in o-800 cm<sup>-1</sup> in order to visualize the temporal dynamics of the CVWP motions obscured by strong THF solvent vibration at 912 cm<sup>-1</sup>. The raw data are provided in Figure S9 (c and d) wavelength-resolved FFT map (top) and spectra (bottom) at specific probe wavelengths for  $\bf 1$  (c) and  $\bf 2$  (d). The FFT was carried out for the residuals within the time range of  $\bf 0.07 - \bf 2.5$  ps to avoid the contribution of cross-phase modulation around time zero.

Chemical Science Page 20 of 48

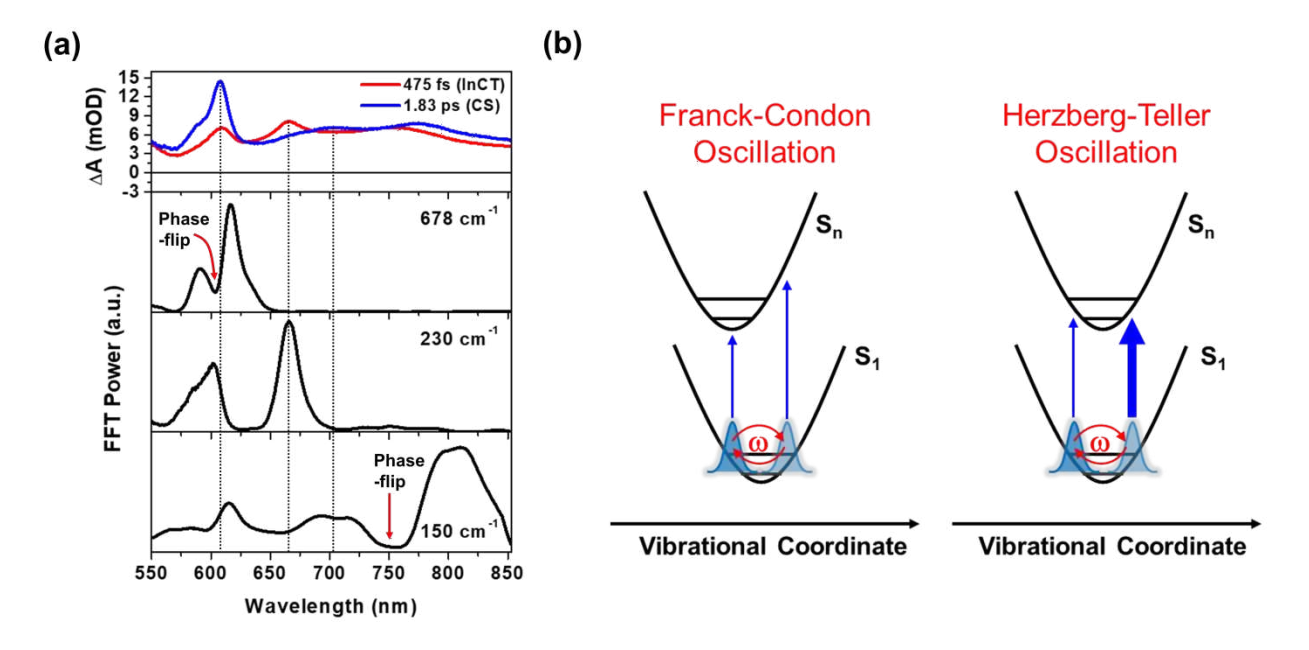


**Figure 4.** (a) FFT amplitude distribution plots for the 678, 230 and 150 cm<sup>-1</sup> modes as a function of probe wavelength. EADSs with the time constants of 475 fs (red) and 1.83 ps (blue) are presented to compare the spectra of intermediate CT (InCT) and CS states with FFT amplitude distribution. Red arrows indicate the spectral position of phase-flip detected in the wavelength-resolved residual map (b) schematic illustration for the two types of CVWP motions: Franck-Condon and Herzberg-Teller type oscillations. The thicker and thinner arrows in Herzberg-Teller type oscillation highlights the difference in oscillator strength between the left and right positions of PES.

Page 21 of 48 Chemical Science

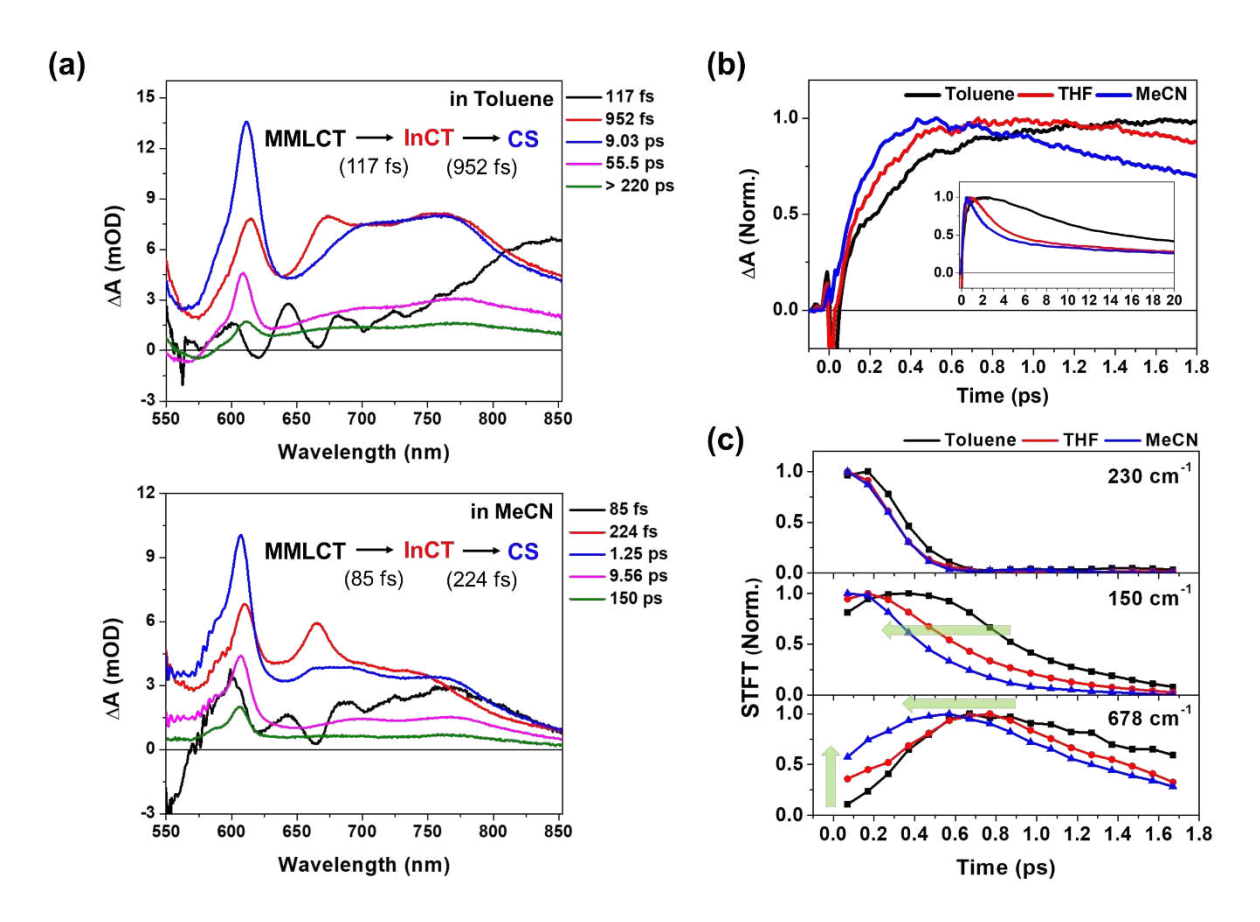


**Figure 5.** (a) EADS for **2** in toluene (top) and acetonitrile (MeCN, bottom), obtained by global kinetic analysis on the BBTA data scanned up to 150 ps (Figure S13). (b) early TA kinetic traces observed at the NDI anion peaks at ~ 608 nm in toluene, THF and MeCN. Inset shows the kinetic traces up to 20 ps. (c) time traces for STFT amplitudes in toluene, THF and MeCN. (top) 230 cm<sup>-1</sup> mode observed at ~667 nm; the STFT amplitudes at each time point were integrated in the frequency range of 200 – 300 cm<sup>-1</sup>, (middle) 150 cm<sup>-1</sup> mode observed at 820 nm, (bottom) 678 cm<sup>-1</sup> mode observed at ~ 615 nm. The green arrows highlight the solvent-polarity dependence in the temporal traces of STFT amplitude for the 150 and 678 cm<sup>-1</sup> modes.

Chemical Science Page 22 of 48

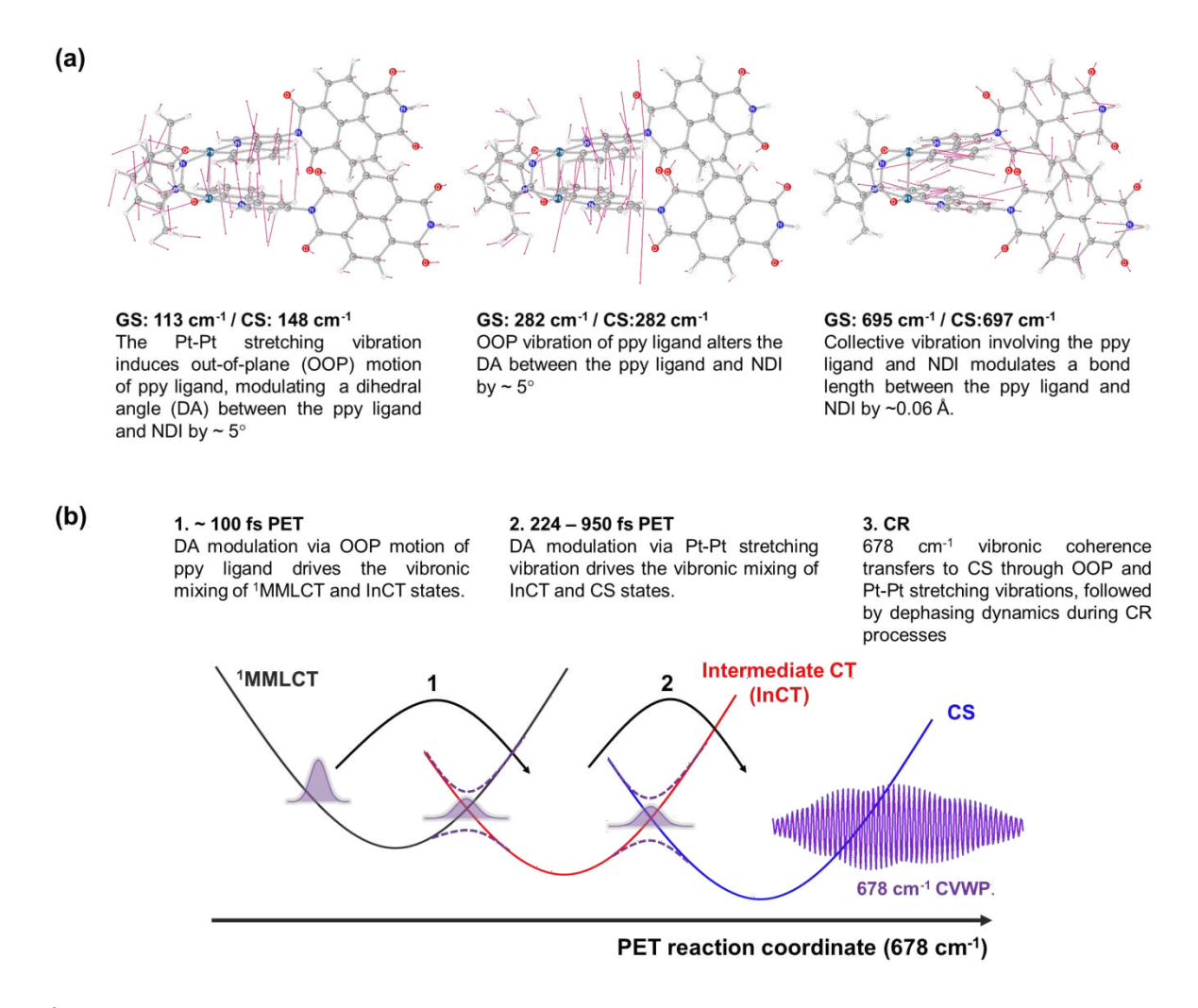


**Figure 6.** (a) calculated normal modes in the ground-state, assigned to 150, 230 and 678 cm<sup>-1</sup> CVWP motions. (b) illustration of PET reaction trajectories.